Check for updates

ENGINEERING

Flexible multichannel muscle impedance sensors for collaborative human-machine interfaces

Junwei Li, Kunlin Wu, Jingcheng Xiao, Tianyu Chen, Xudong Yang, Jie Pan, Yu Chen, Yifan Wang*

The demand for advanced human-machine interfaces (HMIs) highlights the need for accurate measurement of muscle contraction states. Traditional methods, such as electromyography, cannot measure passive muscle contraction states, while optical and ultrasonic techniques suffer from motion artifacts due to their rigid transducers. To overcome these limitations, we developed a flexible multichannel electrical impedance sensor (FMEIS) for noninvasive detection of skeletal muscle contractions. By applying an imperceptible current, the FMEIS can target multiple deep muscles by capturing electric-field ripples generated by their contractions. With an ultrathin profile (~220 micrometers), a low elastic modulus (212.8 kilopascals) closely matching human skin, and engineered adhesive sensor surfaces, the FMEIS conforms nicely to human skin with minimized motion artifacts. The FMEIS achieved high accuracy in both hand gesture recognition and muscle force prediction using machine learning models. With demonstrated performance across multiple HMI applications, including human-robot collaboration, exoskeleton control, and virtual surgery, FMEIS shows great potential for future real-time collaborative HMI systems.

Copyright © 2025 The Authors, some rights reserved; exclusive licensee American Association for the Advancement of Science. No claim to original U.S. Government Works. Distributed under a Creative Commons Attribution NonCommercial License 4.0 (CC BY-NC).

INTRODUCTION

As human-machine interfaces (HMIs) become increasingly prevalent in fields such as domestic robots (*1*, *2*), assistive exoskeletons (*3*, *4*), and virtual reality (VR) (*5*, *6*), the need for sensing interfaces that seamlessly integrate with human physiology has become critical. At the core of these interfaces lies the ability to accurately capture and interpret human muscle activity and its output force. Accurate monitoring of muscle forces is crucial for developing systems that respond naturally to human input, enabling users to control machines through their own muscular movements. However, muscle force is a complex signal influenced by both the muscle's activation level and contraction state (*7*). Electromyography (EMG), especially with recent advances in ultrathin and stretchable electrodes (*8*, *9*) that reduce motion artifacts (*10*), has become a powerful tool for noninvasively assessing muscle activation (*9*, *11*, *12*). Nevertheless, EMG still falls short in capturing the full spectrum of muscle force, as it cannot adequately reflect muscle contraction states. For instance, during joint flexion, antagonistic muscles in a stretched but inactive state still contribute to the overall force exerted yet generate no EMG signals (*13*). Moreover, while substantial progress has been made in developing strong adhesive muscle sensors (*9*), ensuring durable adhesion and consistent performance upon reapplication after removal remains challenging. These challenges have limited the development of wearable sensors capable of accurately measuring muscle forces for seamless integration into HMIs.

Magnetic methods have been investigated to measure muscle contractions but require surgical magnet implantation, posing infection risks (*14*). Optical methods for noninvasively detecting muscle contraction have been explored by measuring changes in light reflection caused by muscle deformations, using light-emitting diodes and photodetectors embedded in a silicone medium (*15*, *16*). However, the rigidity of the probe and the limited measurement depth present notable limitations (*17*). Ultrasonic detection offers another promising approach for assessing deep muscle contractions, particularly with the recent advancements in wearable triggering and sampling modules together with ultrasonic probes (*18*–*21*). While these advances in wearable ultrasonic sensors have effectively reduced device thickness and improved flexibility (*19*, *22*), their application in detecting muscle contraction levels and associated force may be further optimized, partly due to the persistent elastic modulus mismatch between rigid piezoelectric transducers and soft biological tissues, which can still result in motion artifacts (*10*). Electrical impedance measurement (EIM), on the basis of the principle that muscle contraction alters impedance (*23*, *24*), also shows promise for detecting muscle contraction states. EIM involves passing high-frequency milliampere currents through subcutaneous tissue, while multichannel electrodes record the impedance changes during muscle contraction. A major advantage of EIM is that its hardware operates at low current and voltage levels, which is easily integrable into a printed circuit board (PCB) for enhanced portability. Nevertheless, existing EIM-based sensors predominantly rely on rigid, nonstretchable electrodes (*25*–*27*), which fail to accommodate skin deformations, resulting in low wearing comfort and reduced measurement accuracy.

To address these challenges, we present a flexible multichannel electrical impedance sensor (FMEIS) that detects skeletal muscle contractions via impedance sensing, providing high-fidelity physiological information with minimal motion artifacts for wearable human-machine interaction applications (Fig. 1A). By introducing an imperceptible bipolar current (green streamlines; Fig. 1A), the FMEIS captures electrical field perturbations (blue contours; Fig. 1A) caused by muscle geometry and conductivity changes. In contrast to conventional electrophysiological methods that detect only active contractions, the FMEIS can sense both active muscle contraction and passive muscle elongation, thereby enriching the physiological feedback available for advanced HMI. The FMEIS features a 220-μm-thick sensor pad (Fig. 1B) with an elastic modulus of 212.8 kPa, closely matching human skin [420 to 850 kPa (*28*)]. Its low-modulus, high-adhesion design, enabled by a modified polydimethylsiloxane (PDMS) substrate and encapsulation, forms reversible hydrogen bonds with the skin (Fig. 1C), ensuring stable signal quality during prolonged use and enabling reliable reusability without

School of Mechanical and Aerospace Engineering, Nanyang Technological University, 50 Nanyang Avenue, 639798 Singapore, Singapore.
*Corresponding author. Email: yifan.wang@ntu.edu.sg

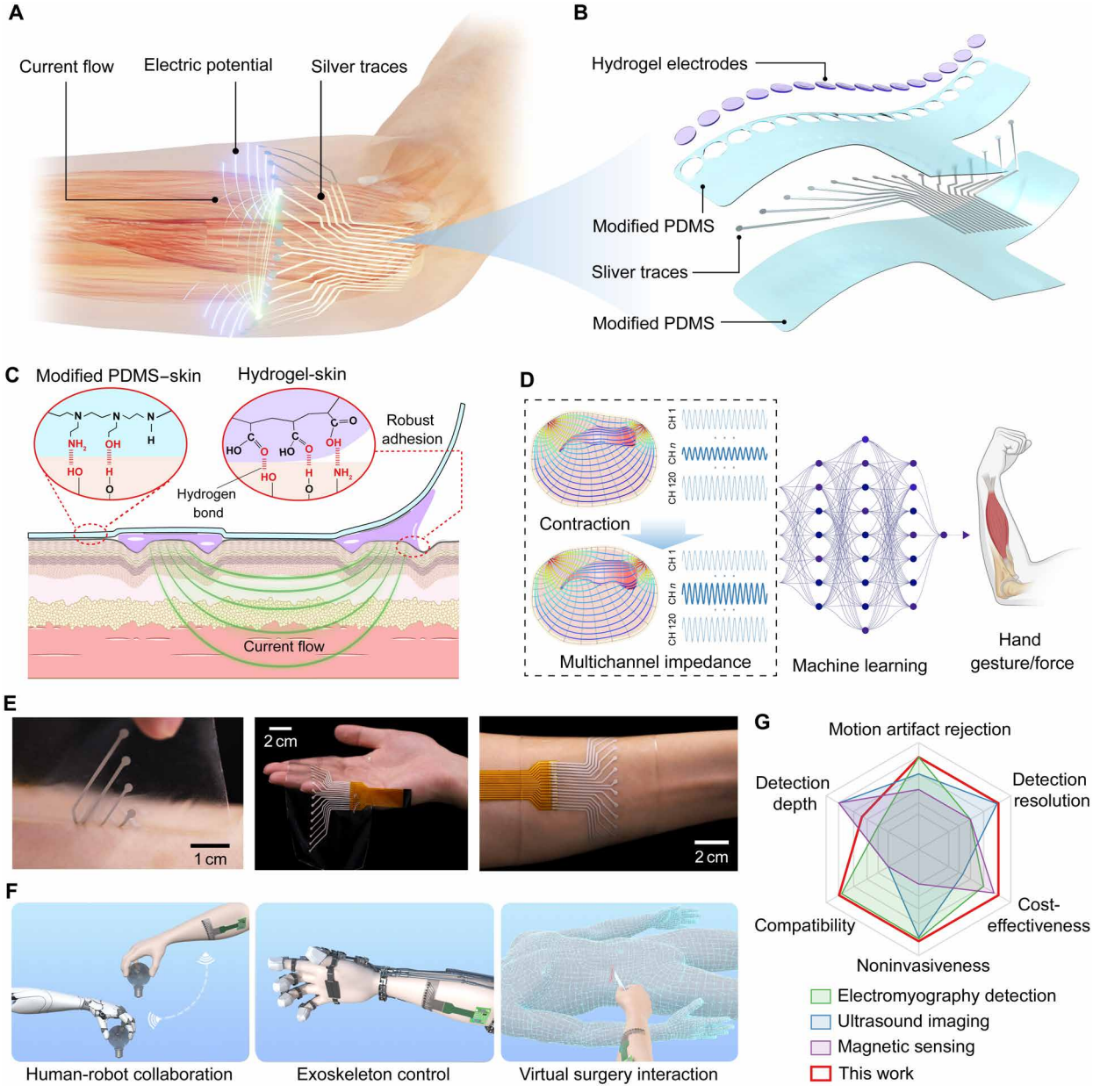


Fig. 1. Overview of the FMEIS for advanced HMI applications. (**A**) Working mechanism of EIM for detecting muscle contraction states. (**B**) Design of the FMEIS sensor pad with good stretchability and adhesion. (**C**) Adhesion forces between the modified PDMS layer and the skin, as well as between the hydrogel and the skin, attributed to hydrogen bonds. (**D**) Predicting muscle activities from the electric-field ripples detected across multiple channels using FMEIS. CH, channel. (**E**) Photos demonstrating the wearability and flexibility of the FMEIS. (**F**) Three application scenarios for FMEIS as HMIs: human-robot collaborations based on FMEIS measurements (left), an exoskeleton controlled by FMEIS worn on the human forearm (middle), and a virtual surgery interface controlled by measurements from FMEIS (right). (**G**) Comparison of motion artifact rejection, detection depth, detection resolution, compatibility, cost-effectiveness, and noninvasiveness among different muscle contraction detection methods (*9*, *11*, *14*, *19*, *21*). Compatibility means that the method can cooperate with other methods. A quantitative comparison can be found in table S2.

noticeable loss of adhesion. Conductive hydrogel electrodes reduce contact impedance and further improve signal stability. Stretchable circuits embedded in the pad tolerate up to 50% strain without compromising signal integrity. The system includes a lightweight 4-g sensor pad and a 53-g control unit, which processes multichannel impedance data using machine learning algorithms for gesture classification and muscle force prediction (Fig. 1D). On the basis of the engineered thin adhesive sensor pad (Fig. 1E), the system achieved an accuracy of 98.49% in hand gesture classification and a coefficient of determination (R^2) of 0.98 in muscle force prediction. The demonstrated high detection accuracies support the reliable performance of the FMEIS across multiple HMI applications, including human-robot collaboration, exoskeleton control, and virtual surgery (Fig. 1F). To further illustrate the key advantages of the FMEIS, we compiled a performance comparison of various muscle contraction detection methods in terms of motion artifact rejection, detection

depth, resolution, compatibility, cost-effectiveness, and noninvasiveness (Fig. 1G). Furthermore, the FMEIS exhibits strong compatibility with complementary sensing methods such as EMG, offering a comprehensive approach to muscle force detection.

RESULTS

Design and characterizations of FMEIS

The sensor pad of the FMEIS (Fig. 1B) consists of an elastic conductive trace layer, two modified PDMS encapsulation layers, and an electrode layer made of ultraviolet (UV)–cured hydrogels. To gain good conformability with human skin, we fine-tuned the fabrication processes of all layers (Fig. 2A and Materials and Methods) to achieve a low elastic modulus, strong adhesion, and minimal thickness. The conductive trace layer consists of 16 silver-polyurethane traces with an average thickness of 30 μm. With a total sensor pad thickness of 220 μm, the design is sufficiently thin to enhance wearability. The skin-facing encapsulation layer is made from PDMS modified with ethoxylated polyethylenimine (PEIE) to expose more hydroxyl groups and reduce the modulus (*29*). These exposed hydroxyl groups are highly polar, allowing the formation of strong, reversible hydrogen bonds (Fig. 1C) with polar molecules in the skin, such as water, proteins, and lipids. The electrodes are composed of a double-network acrylamide (AAm)/acrylic acid (AAc) conductive hydrogel, selected for the toughness of AAm and the adhesive properties (Fig. 1C) of AAc (*30*). This combination ensures that the electrodes remain stable on the skin without breaking under considerable strain. The addition of sodium chloride (NaCl) to the hydrogel further reduces electrode-skin contact impedance, resulting in a resistance of 1227.3 ± 17.1 ohms (50 kHz) for a pair of hydrogel electrodes spaced 15 mm apart on clean skin, within a suitable range for the muscle EIM. In addition, the ability of the conductive traces to withstand stretching deformation was evaluated. As shown in fig. S1, the resistance of a straight conductive trace (measured at 50 kHz) on the modified PDMS under varying tensile strains changed from 20.4 to 107.8 ohms for strains below 50%, remaining considerably lower than the hydrogel-skin contact impedance (1227.3 ohms). Localized cracks appeared at strains exceeding 30%, with the trace breaking at strains greater than 66.7%. Given that the average strain experienced at the midpoint of the human forearm is ~23% during movements (*31*), the conductive traces are fully capable of accommodating the deformations encountered in the skin during typical human movements.

To evaluate the wearability of the sensor pad, we experimentally characterized its elastic modulus and adhesion force. Because the PDMS encapsulation layers cover most of the sensor area, the elastic modulus of the sensor pad is close to that of the PDMS encapsulation layer. A tensile test performed on the modified PDMS yielded an elastic modulus of 212.8 kPa (fig. S2 and note S1). This value is slightly smaller than that of human skin, which typically ranges from 420 to 850 kPa (*28*). The adhesive properties of both the modified PDMS and the hydrogel were evaluated using standard 180° peeling tests on soda-lime glass. The results (Fig. 2B) indicate an adhesion force of 12.41 N/m for the modified PDMS and 14.28 N/m for the hydrogel, calculated from average values of the shaded plateau regions in Fig. 2B. For comparison, commercial medical tapes generally exhibit adhesion forces between 15.75 and 110 N/m (*32*). These results indicate that both the modified PDMS and hydrogel provide strong yet nonexcessive adhesion, ensuring stable contact while maintaining ease of removal, which is crucial for HMI applications involving repeated skin contact and removal. The low modulus and excellent adhesion of the sensor pad help reduce stress concentration at the electrode-skin interface, minimizing relative movement during human movements and providing excellent motion-artifact rejection ability (Fig. 1G). To evaluate the durability and reusability of the adhesive sensor pad, we performed peeling tests on human skin over an 8-hour period and on a freshly prepared sensor pad over five consecutive days of reuse. The results over the 8-hour period (Fig. 2C) indicate that the adhesive force slightly decreased from 12.73 to 9.8 N/m, primarily due to sweat accumulation. Figure 2D demonstrates that the adhesiveness of the FMEIS surface remains effective over several days, exhibiting only a minor decrease from 13.57 to 10.55 N/m after daily usage of ~3 hours. Collectively, the results shown in Fig. 2 (C and D) confirm the durability and reusability of the sensor pad, providing the basis for the long-term stable monitoring of muscle contractions presented later.

To illustrate the mechanism of using muscle impedance to measure muscle contraction, Fig. 2E provides a numerical analysis of the electric-field measurements during muscle deformation. For the forearm cross section (*33*) shown on the left of Fig. 2E, the FMEIS with 16 electrodes was attached, with a current of 50-kHz frequency and 0.4-mA amplitude applied between the 4th and 12th electrodes. When the brachioradialis (BR), flexor digitorum superficialis (FDS), and flexor carpi ulnaris (FCU) muscles contract, the forearm cross section deforms according to mechanical principles, distorting the electric field in the muscles relative to its original state. This distortion causes changes in the electric potentials measured at the 16 electrodes. The full parametric settings (*33*, *34*) of the simulation are detailed in note S2. The three subfigures on the right of Fig. 2E depict the electric potential changes across the 16 electrodes, revealing that the largest electric potential changes occur in skin areas closest to the contracting muscles. This illustration suggests that the contraction state of the underlying muscles can be inferred from the voltage measurements at the FMEIS electrodes.

To assess the repeatability and stability of using the impedance measurements to infer muscle contraction, we conducted tests on a human participant using a 50-kHz sinusoidal current at 0.4 mA, a parameter also used in the subsequent multichannel impedance measurements. For the assessment, we used the four-point measurement configuration (Fig. 2F), which minimizes the influence of contact impedance fluctuations by separating the current injection electrodes from the voltage measurement electrodes (see explanation in note S3). During the measurement, the participant wearing the FMEIS alternated wrist flexion and extension every 10 s over a 13-min period. As the current source maintained a constant amplitude, the measured voltage changes directly corresponded to impedance variations. The measured impedance curve shown in the bottom of Fig. 2F revealed distinct differences between wrist flexion and extension and demonstrated good repeatability over 38 cycles during the 13-min session. Because of its low elastic modulus and durable adhesion, the sensor pad is suitable for long-term stable monitoring of muscle contractions and is reusable over multiple days. As illustrated in fig. S5A, impedance signals recorded during an 8-hour continuous use without hydrogel replacement, and over five consecutive days with hydrogel electrodes replaced once daily before each use, exhibited only minor drift in certain channels, mainly due to slightly reduced adhesion caused by sweat accumulation. In addition, fig. S5B demonstrates that strong hydrogen bonds

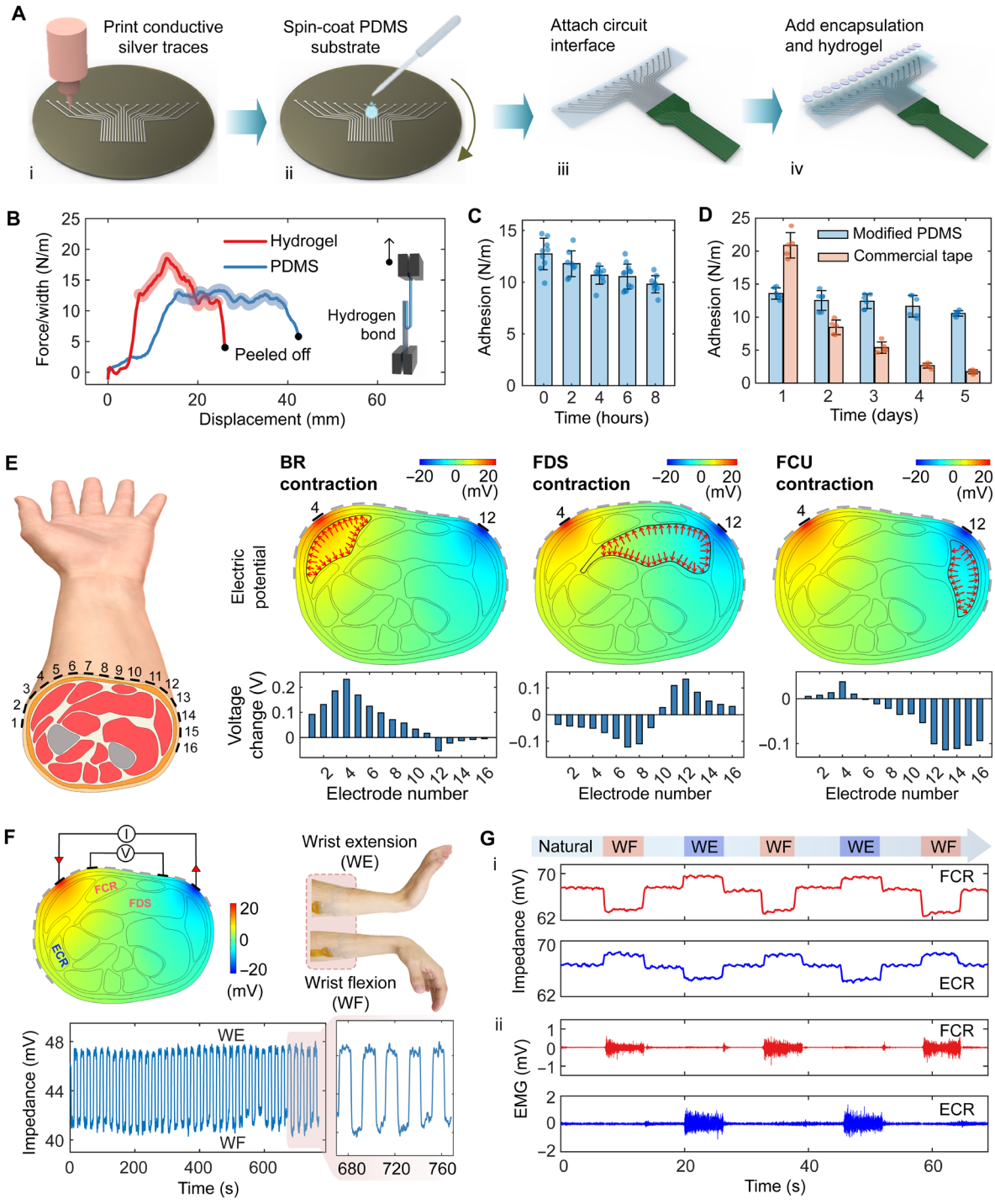


Fig. 2. Fabrication process, characterization, working principle, and measurement results of the FMEIS. (**A**) Fabrication procedure of the different layers in the sensor pad. (**B**) Adhesion force of hydrogel (electrodes) and modified PDMS (encapsulations) during peeling test on glass. The inset shows the configuration of the peeling test where the glass and one end of the tested material were clamped. (**C**) Adhesion force of the modified PDMS on human forearm skin measured over 8 hours (obtained via 90° peeling tests). (**D**) Adhesion force of the modified PDMS compared with a commercial thermoplastic polyurethane (TPU) tape (Hons Medical) on human forearm skin measured over 5 days. Both the modified PDMS and TPU tape were tested once daily. (**E**) Simulation of electric fields and voltage measurements when three muscles in the forearm contract: brachioradialis (BR), flexor digitorum superficialis (FDS), and flexor carpi ulnaris (FCU). The three figures in the top right are the electric fields in forearm tissues. The three figures in the bottom right are the voltage changes across all 16 electrodes. (**F**) Simulated electric potential field in four-point impedance measurement configuration (top) and the experimental recorded four-point impedance data (bottom) when the human participant repeatedly conducted wrist extension and flexion for 13 min. The shaded area beneath the hand photo indicates the sensor position. (**G**) Comparison between impedance signals measured using FMEIS and EMG signals measured using commercial EMG sensors. The sensors were placed on skin sites above the flexor carpi radialis (FCR) and extensor carpi radialis (ECR) muscles.

between the sensor pad and the skin could still effectively reform, even after the sensor had been repeatedly peeled off and reapplied with freshly replaced hydrogel electrodes. The robust repeatability and durability of the adhesive, soft, and thin FMEIS establish a solid foundation for classifying hand gestures and estimating muscle forces based on muscle contraction states.

To demonstrate the advantage of FMEIS over traditional EMG sensors, we experimentally compared their detection capacities. In the experiment, the FMEIS was attached to the participant's forearm, covering the skin sites above the flexor carpi radialis (FCR) and extensor carpi radialis (ECR) muscles (Fig. 2F). Four adjacent electrodes within the 16-electrode FMEIS located over the FCR muscle were used to form a four-point impedance measurement configuration to capture FCR activities, while another group of four neighboring electrodes was used to monitor the states of the ECR muscle. The participant performed repeated wrist flexion and extension motions as indicated by the labeled arrow in Fig. 2G. The impedance data collected from the two groups of electrodes are presented in Fig. 2Gi. The red curve, representing impedance measured by the electrode group over the FCR, reflects both active contractions (lower plateaus in Fig. 2Gi) and passive stretches (higher plateaus in Fig. 2Gi) of the FCR muscle. Similarly, the blue curve represents impedance measured by the electrode group over the ECR and accurately captures both its active contractions and passive stretches. For comparison, EMG signals from the FCR and ECR muscles during wrist flexion and extension movements were recorded using two commercial EMG sensors (Materials and Methods) placed on these muscles (Fig. 2Gii). The EMG signals from the FCR exhibited no electrical activity when the muscle was passively stretched during wrist extension. Likewise, the ECR muscle displayed no electrical activity when passively stretched during wrist flexion. These results (Fig. 2G) demonstrate that the FMEIS method effectively measures both active and passive muscle motions, overcoming the inherent limitation of traditional EMG sensors, which can detect only active contractions. Regarding the performance metrics of FMEIS shown in Fig. 1G, we provided quantitative comparisons in table S2, along with a detailed discussion in note S4. Specifically, FMEIS has been demonstrated to detect various hand gestures (two wrist motions and independent flexions of five fingers) actuated by muscles located at various depths (fig. S7 and movie S1). The experimental results show a maximum detection depth of ~30 mm, which closely aligns with the numerical simulation result of around 35 mm (fig. S6 and note S4). Additional discussions on the other performance metrics are also provided in note S4.

Impedance data mining for gesture and muscle force measurements

Using the fabricated sensor pad, the driving/sampling PCB (Fig. 3A) of the FMEIS can acquire multichannel impedance data for analyzing human hand gestures and muscle forces. The "opposite" configuration (*35*), a commonly used method in EIM, was used. In this configuration, a pair of opposite electrodes (such as the first and ninth electrodes for the 16-electrode system) is selected as the current injection pair, while the remaining electrodes are used to measure the resulting voltage differences. By programmatically controlling the multiplexers on the PCB, 120 independent impedance values were measured from 16 electrodes per frame (note S5). These 120 independent impedance values form an impedance pattern, which updates every 127 ms and can be transmitted to remote devices via the onboard Bluetooth module. The continuous stream of impedance patterns was first used to classify 10 frequently used hand gestures. Because the muscles responsible for finger and wrist flexion are primarily located in the medial forearm, the sensor pad was placed on the skin in this area (Fig. 3A). For each gesture, a series of impedance patterns was collected for machine learning training. Given the high sampling rate of 127 ms per frame, the entire training data collection process for 10 gestures took only 2.2 min. To evaluate the quality of the training data, we used principal components analysis to extract the distribution features of the impedance data in a low-dimensional space. Figure 3B illustrates the three dominant principal components of all impedance patterns in the training dataset, revealing clear boundaries for each gesture. These results indicate a strong potential for gesture classification using machine learning algorithms.

Before feeding the training dataset into the classification model, automatic feature selection was applied using one-way analysis of variance [ANOVA (*36*) and note S6] to account for variability under contact conditions and signal quality across different electrodes (note S3). A fully connected neural network, featuring a single hidden layer of 25 nodes, was then used as the classification model (note S7). To validate the trained model, the participant performed various hand gestures, and the corresponding impedance patterns were measured for gesture estimation. Figure 3C shows the classification accuracy of one participant for each gesture with an overall accuracy of 98.22%, demonstrating strong performance for further HMI applications. Figure 3D visualizes the effective impedance patterns extracted using the feature selection process during both training and testing. As a result, all impedance patterns acquired from various hand gestures are represented as stacked colored lines, with the horizontal axis representing the channel number in a single impedance pattern (Fig. 3D). The result highlights the high repeatability of the FMEIS, as evidenced by the waveform similarity across multiple repeated measurements for different hand gestures.

Moreover, the capability of the FMEIS to detect human muscle force was experimentally validated using a pinch action as a test case. Because this action activates multiple muscles, including the FDS, the sensor pad was attached to the skin above the FDS muscle belly. Pinch force data were collected from a rigid force sensor using a customized clamp (Fig. 3E), covering seven force levels ranging from 0 to 30 N, with data collection completed in 90 s. A quadratic support-vector machine, a machine learning algorithm that maps data into a higher-dimensional space to identify patterns, was used as the force regression model (note S7). Unlike the gesture classification task, the *F* test method (note S6) was used for automatic feature selection to generate an effective impedance pattern. To evaluate the trained regression model, we collected impedance patterns at various force levels. As shown in Fig. 3E, the regression results demonstrated an R^2 of 0.97 between the predicted and true pinch forces, with a root mean square error (RMSE) of 1.61 N. In Fig. 3F, the first 22 dominant impedance values extracted through feature selection show a distinct shift in impedance patterns, as pinch force increased from 0 to 30 N. These regression analyses indicate that the FMEIS demonstrates strong potential for accurately measuring muscle forces in HMI applications.

To further validate the robustness and generalizability of the FMEIS method across individuals, we conducted gesture classification and muscle force regression analyses with three participants. In addition to the data from participant 1 presented in Fig. 3, results for

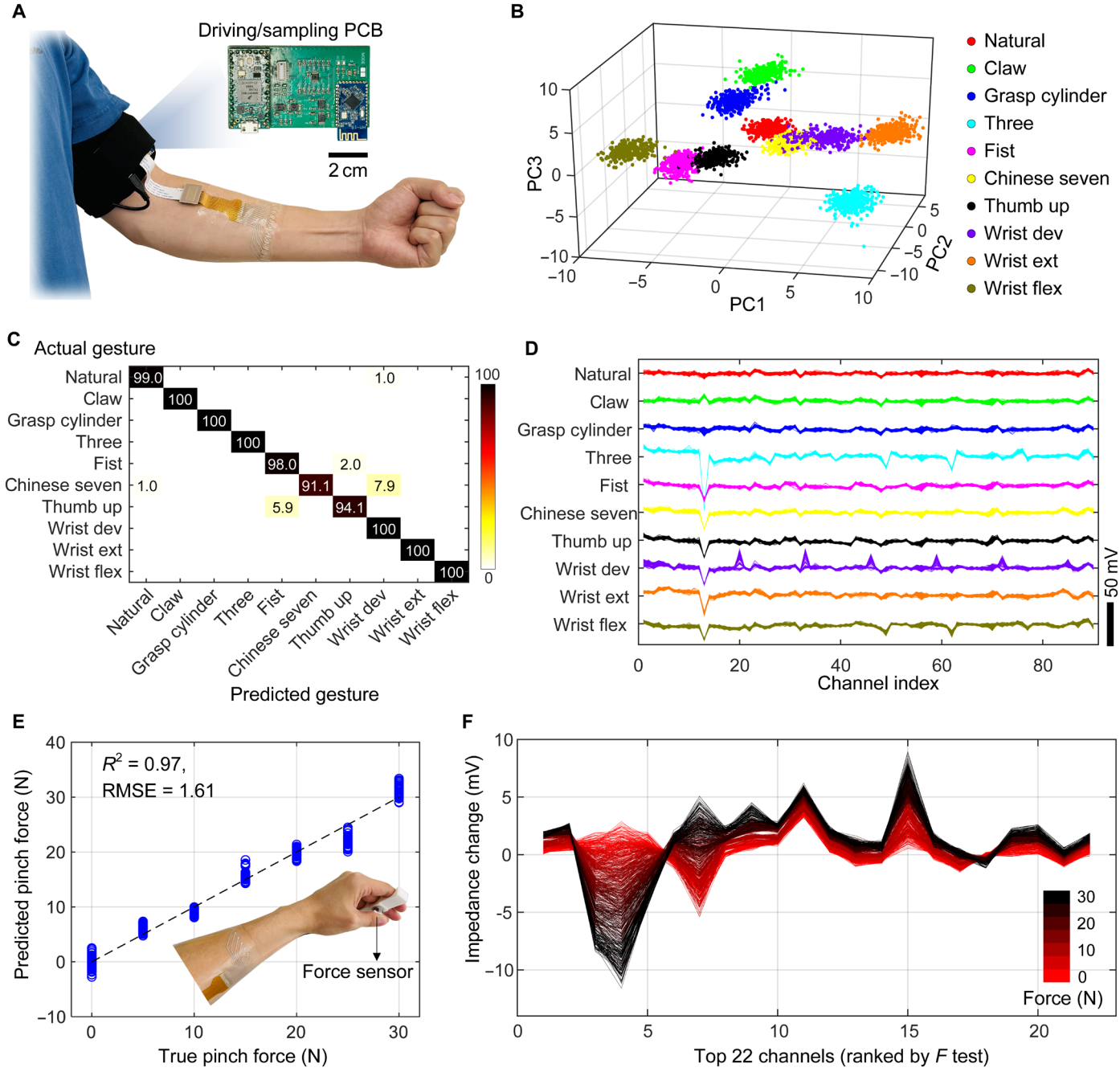


Fig. 3. Hand gesture classification and force regression using the FMEIS. (**A**) Wireless FMEIS worn on a human participant's forearm. The sampling PCB along with its battery was fixed on the participant's arm by a comfortable fabric armband. (**B**) Three dominant principal components (PC) of impedance pattern data for different hand gestures. Wrist (dev, ext, and flex) represents wrist (deviation, extension, and flexion). (**C**) Gesture prediction result using the muscle impedance data measured by FMEIS. (**D**) Repeated impedance pattern data for all 10 gestures. The horizontal axis represents the channel number in the impedance pattern. (**E**) Linear regression plot between the true and predicted pinch forces. The subfigure shows how the true pinch force was measured by a force sensor. (**F**) Impedance pattern data measured by FMEIS for seven force levels. The horizontal axis represents the top 22 channels selected using the *F* test method.

participants 2 and 3 are shown in fig. S10. The average gesture classification accuracy was 98.49% (±0.46%), and the mean R^2 value for muscle force regression was 0.98 (±0.01), demonstrating strong robustness against variations in skin impedance and adipose tissue thickness. Building on the validated ability of the FMEIS to accurately classify hand gestures and estimate muscle forces, this sensor system is poised to address the limitations of other technologies, such as vision- and inertial-based sensors, by capturing subtle yet critical information during human-machine interactions. To demonstrate its great potential, the FMEIS will be applied in three HMI scenarios, as described below. The machine learning models and training methods used in these applications are consistent with those discussed earlier in this section.

Human-robot collaboration interface

With the rapid advancements in robotics, ensuring safe and collaborative human-robot interactions has become increasingly crucial. This section demonstrates the FMEIS's capability to classify hand gestures and estimate muscle forces for effective human-robot collaboration. In the experimental setup (Fig. 4A), a human participant and a robotic hand-arm system worked together to install screws onto a motor transmission assembly. The FMEIS, worn on the participant's forearm, detected impedance patterns, which were transmitted to a host computer for real-time gesture classification and force regression. The host computer then used this information to control the robotic hand-arm, executing tasks via a customized real-time program.

In human-robot collaboration, human hand activities can serve as effective control commands for the humanoid robotic hand-arm systems due to their structural and size similarities, enabling precise control in tool grasping and working posture adjustments. We tested the ability to manipulate the robotic hand-arm using human hand gesture information analyzed by the FMEIS. Five gestures and three grasping modes were tested, engaging the robotic system's eight degrees of freedom (df). The manipulation performance is illustrated in Fig. 4B and movie S2. The robotic hand-arm accurately followed all tested human actions with a mean latency of 0.46 s (movie S2), primarily attributed to the moving-average filter used in data processing, communication delay, and the mechanical response time of the robotic system.

Building on the successful control of the robotic hand-arm using FMEIS data, the next step was to achieve collaboration between the human participant and the robotic system in complex tasks, leveraging the sensor information for synchronized and intuitive interaction. In this human-robot collaboration experiment, the human securely held an irregularly shaped assembly part, while the robotic hand-arm operated an electric screwdriver to install screws onto it (Fig. 4A). For the robotic hand-arm to perform its task safely, it needed to detect the clamping force applied by the human hand, ensuring that it proceeded with installation only when it was safe

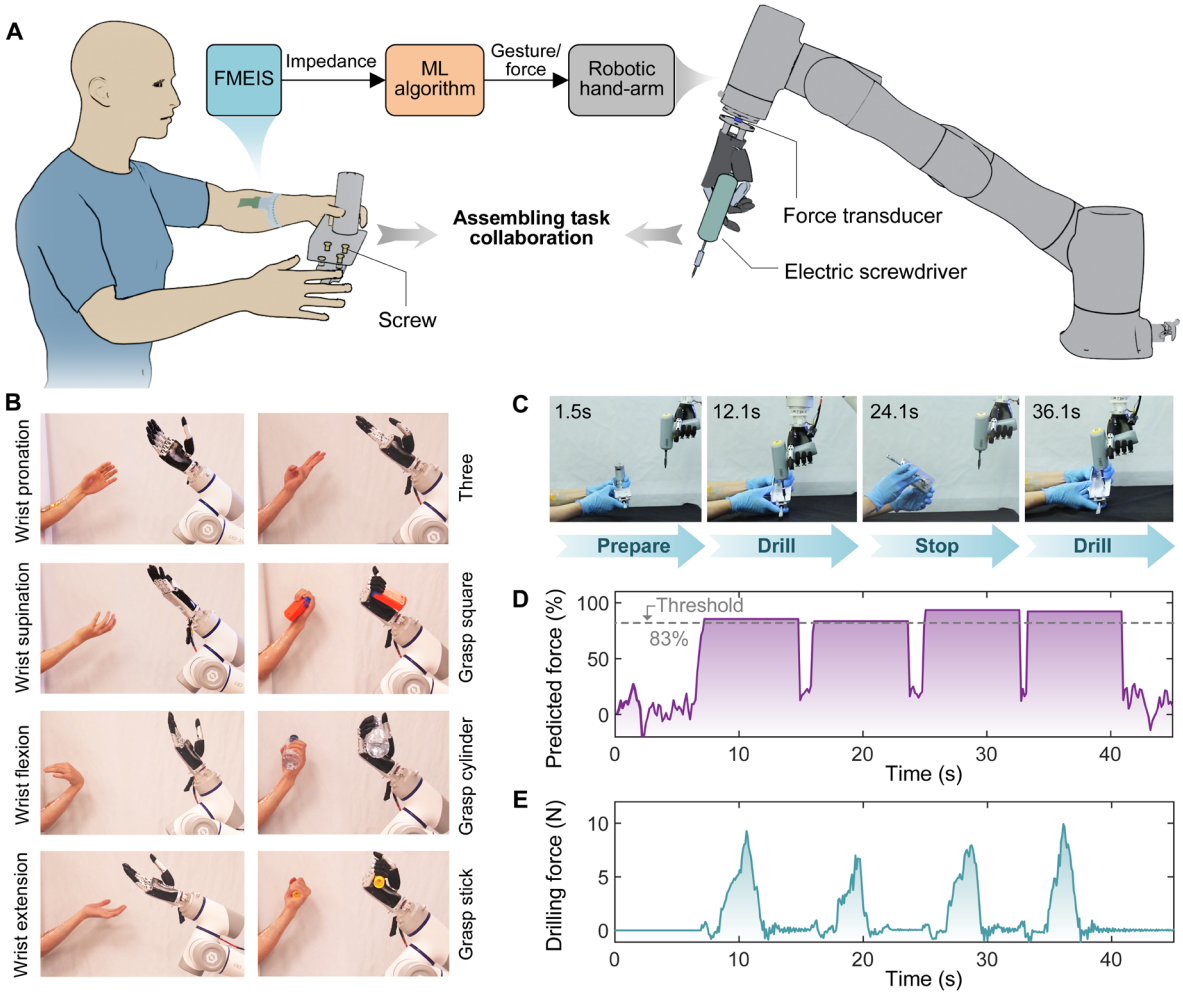


Fig. 4. Human-robot collaboration using FMEIS. (**A**) Schematics illustrating the collaborative assembly task between a human participant holding an irregularly shaped assembly part and a robotic hand-arm holding an electric screwdriver. (**B**) Robot gestures and grasping modes controlled by a human participant wearing FMEIS. (**C**) Four representative frames during the human-robot collaboration process. The time stamps are labeled in the top left corner of each frame. (**D**) Human clamping force predicted by the FMEIS (normalized to a maximal value of 40.7 N during calibration). The dashed line indicates the clamp-force threshold preset for initiating the robotic drilling. (**E**) Robotic drilling force when assembling screws onto an assembly measured by the force transducer installed in the base of the robotic hand.

to do so, minimizing risk to the human operator. The FMEIS played a crucial role in providing real-time data on the human hand's clamping force to ensure safety. A full recording of the collaboration process using FMEIS is demonstrated in movie S3, and four representative frames of the collaboration are presented in Fig. 4C to demonstrate the different working stages. For quantitative analysis, the predicted clamping force from the FMEIS and the drilling force of the robotic hand-arm during the collaboration are shown in Fig. 4 (D and E). To ensure safety, the threshold for initiating drilling was set at 83% of the human participant's maximum clamping force (Fig. 4D). As shown in the four peak areas in Fig. 4E, the robotic hand-arm only initiated drilling when the human-applied force exceeded this threshold. The FMEIS measurements paused temporarily after the measured clamping force exceeded the threshold, resuming only after the drilling process was completed, which kept the predicted clamp force constant during drilling (Fig. 4D).

The human-robot collaboration experiment underscores the advantages of the FMEIS over traditional human posture sensors. In scenarios involving potentially harmful contact forces during human-robot interaction, visible changes in human posture may be minimal, while strong muscle contractions occur to resist these forces. Conventional posture sensors (*37*, *38*) may struggle to detect such subtle postural adjustments, whereas the FMEIS excels at capturing and transmitting critical muscle contraction information to the robot. This capability enhances the robot's ability to respond appropriately according to human muscle forces, thereby reducing the risk of dangerous interactions.

Exoskeleton control for human assistance

The ability of FMEIS to estimate muscle force provides essential information for exoskeleton control. As illustrated in Fig. 5A, the muscle force predicted by FMEIS was used to modulate the output force of a pneumatic hand exoskeleton by adjusting the input voltage to a pressure-regulating valve. To demonstrate the force-tracking performance of the FMEIS-based control method, we conducted a four-finger grasping test, with both the participant's hand and the exoskeleton gripping a force sensor. Figure 5B shows the measured grasping forces from both the human hand and the exoskeleton. The two force curves exhibit very similar trends, with the exoskeleton's output force showing a slight latency, averaging 756 ms, relative to

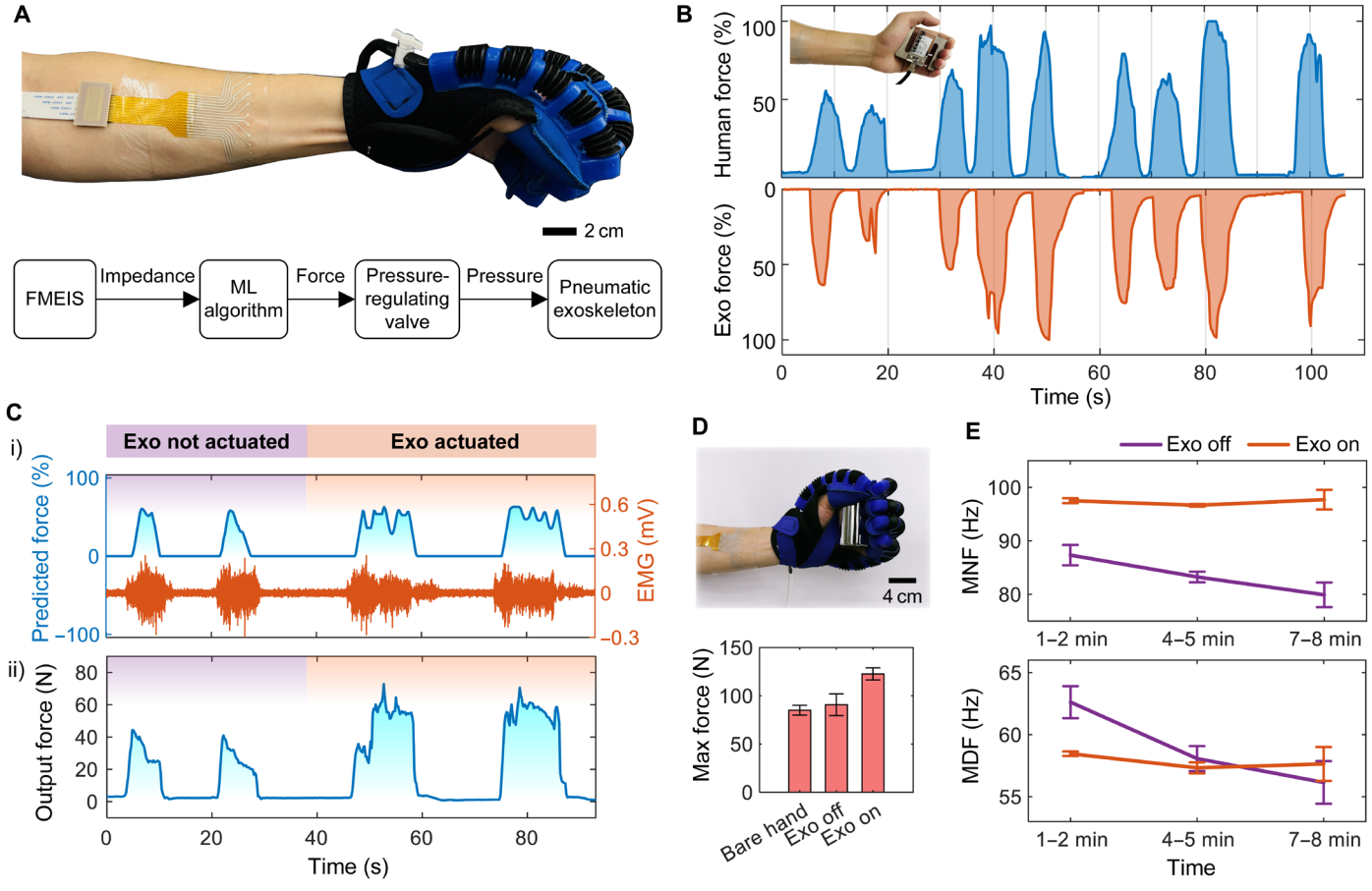


Fig. 5. Assistive exoskeleton controlled using muscle force predicted by FMEIS. (**A**) Pneumatic hand exoskeleton and its control flowchart based on impedance patterns measured by FMEIS. ML, machine learning. (**B**) Grasping forces of the participant's bare hand and the exoskeleton controlled using muscle force predicted by FMEIS. The two forces are normalized to their maximal values (80.0 and 44.5 N) during calibration. "Exo" refers to the exoskeleton. (**C**) Effect of FMEIS-based control method on human-exoskeleton output force: (i) Predicted hand grasping force by FMEIS (normalized to a maximal value of 90.7 N during calibration) and the corresponding muscle EMG signal measured by a commercial sensor and (ii) total output force of the hand-exoskeleton system. (**D**) Maximum grasp force achieved by the participant under three conditions: bare hand, wearing the deactivated exoskeleton, and wearing the FMEIS-controlled exoskeleton. (**E**) Muscle fatigue analysis using mean and median frequencies of EMG while the participant held a 1-kg weight.

the human grasp force. It is anticipated that incorporating predictive algorithms (*39*) could further reduce this latency.

To evaluate the assistance performance of the FMEIS-controlled exoskeleton, we considered two scenarios (Fig. 5C): one where the exoskeleton remained unactuated, and another where the exoskeleton was actuated on the basis of the human force predicted by the FMEIS. For comparison, a commercial EMG sensor was attached to the FDS to provide insights into muscle activation during grasping. Notably, the FMEIS and EMG sensors can operate simultaneously without interference due to their sufficiently separated operating frequency ranges. Figure 5Ci displays the predicted human force from the FMEIS and the corresponding raw EMG signal when the participant intermittently applied four periods of moderate grip forces, while Fig. 5Cii shows the output force of the human hand while wearing the exoskeleton. The exoskeleton transitioned from deactivated to activated at 38 s, as shown by the boundary between the purple and orange regions. As seen in Fig. 5C, despite similar muscle activation levels before and after exoskeleton actuation, as indicated by the EMG amplitudes, the peak output force increased by 65%, from 44.2 to 72.8 N. The maximum four-finger grasping force of the participant's hand while wearing the exoskeleton is presented in Fig. 5D, demonstrating an increase in maximum force from 85.1 N (bare hand) to 122.7 N with exoskeleton actuation.

Besides force augmentation, the FMEIS-controlled exoskeleton also demonstrates strong potential in mitigating muscle fatigue. Two metrics—mean frequency (MNF) and median frequency (MDF) of the muscle EMG signal—were used to evaluate the impact of the FMEIS-controlled exoskeleton on muscle fatigue. Decreases in MNF and MDF are widely accepted as indicators of muscle fatigue (*40*). We tracked the temporal variation of these two metrics as the participant held a 1-kg weight for 8 min. The results in Fig. 5E indicate that the FMEIS-controlled exoskeleton effectively prevented the decline in MNF and MDF, underscoring its positive impact on reducing muscle fatigue. The results in Fig. 5 highlight the substantial advantages of FMEIS in exoskeleton control. By monitoring muscle contractions with an ultrathin sensor pad, FMEIS avoids interference with the exoskeleton actuators while delivering reliable muscle force predictions. In addition, it reduces muscle fatigue, enhances exoskeleton responsiveness, and improves user comfort, offering a robust solution for human-in-the-loop exoskeleton control applications.

Virtual surgery interface

Since the advent of medical robotics in the mid-1980s, remote robot-assisted surgeries have gained widespread attention for their ability to improve surgical precision, enhance a surgeon's dexterity, and extend advanced medical care to remote locations (*41*). These surgeries rely on a robust VR environment where the surgeon's hand posture and applied forces are accurately captured and transmitted as control inputs. The FMEIS contributes a crucial role to this process by serving as a highly effective interface between the surgeon and the VR system, providing detailed information about hand posture and muscle forces. Figure 6 presents an experimental demonstration of virtual surgery conducted using the FMEIS as the interface. In this VR setup, the surgeon's hand movements, the motion of the surgical knife, and the deformation of the patient's skin were programmatically controlled on the basis of real-time data measured by the FMEIS. To simulate patient skin, we placed a PDMS-based skin phantom, chosen for its similar elastic modulus to that of human skin, on an adjustable platform set at a comfortable orientation for the cutting task. The human participant used a surgical knife to incise the skin phantom, while the FMEIS, worn on the forearm, measured muscle contractions and analyzed the real-time hand posture and cutting force. A demonstration of the predicted hand posture adjusting the view angle in the VR environment is shown in movie S4. Once the optimal view angle was set, the cutting force predicted by the FMEIS controlled the subtle hand motion of the cutting procedure in the VR environment (Fig. 6A).

A demonstrative video showing both the real-world and VR incision processes is available in movie S4. For quantitative evaluation, the cutting force predicted by the FMEIS in the real world is shown in Fig. 6B, which is normalized to the maximal cutting force of 14.3 N measured by a force sensor. On the basis of the predicted muscle force, a customized algorithm (note S8) was used to estimate the cutting length and width (Fig. 6C), which were then applied to update the virtual incision process. For quantitative comparison, the real-world cutting length and depth captured by a camera are presented in Fig. 6D as a benchmark. Figure 6 (C and D) shows four cutting periods (i to iv) with nearly identical initiation and termination times. In Fig. 6 (B to D), the four cutting periods correspond to four distinct increases in cutting length (e.g., 8.8 to 16.2 s), while the cutting length remained unchanged during intervals with no applied force (e.g., 16.2 to 24.2 s). In addition, the cut width was closely correlated with the predicted input force at the knife tip's current position (Fig. 6C), leading to a dynamically varying width along the entire cut trace. This capability for fine-tuned control enables surgeons to execute precise and dexterous cutting operations during remote robot-assisted surgeries. Figure 6 (D and E) displays real-world cutting scenes and the corresponding virtual cutting scenes at five successive time points, where the virtual scenes were updated using the estimated cutting length and width (Fig. 6C). The motion of the virtual surgeon's hand closely followed that of the human participant, initiating the virtual skin incision when the real hand began cutting the skin phantom and halting when the real hand stopped. While the overall trends in cutting length are consistent in Fig. 6 (C and D), noticeable differences in cut width and depth, both of which are force dependent, can still be observed. These discrepancies likely arise from the challenge of maintaining identical muscle recruitment patterns during the cutting tests and the regression model training sessions, particularly given that the wrist involves three df. To further improve force regression accuracy in complex motions, future work may involve collecting a broader range of impedance data across diverse wrist movements, applying more precise labeling strategies, and incorporating advanced machine learning algorithms.

The results in Fig. 6 highlight the unique advantage of FMEIS in virtual surgery scenarios, where the surgeon's muscle force is directly transmitted to the VR environment. Integrating the FMEIS with a haptic feedback device such as a haptic glove (*42*) could allow for bidirectional transmission of motion and force between the user and the virtual environment. This bidirectional information exchange would eliminate the need for physical setups such as skin phantoms, making it possible to fully integrate virtual surgery systems into wearable devices, thereby enhancing the performance of robot-assisted surgeries and other remote-control applications.

DISCUSSION

In this work, we introduce FMEIS, a wearable FMEIS capable of capturing both active and passive muscle contractions, providing

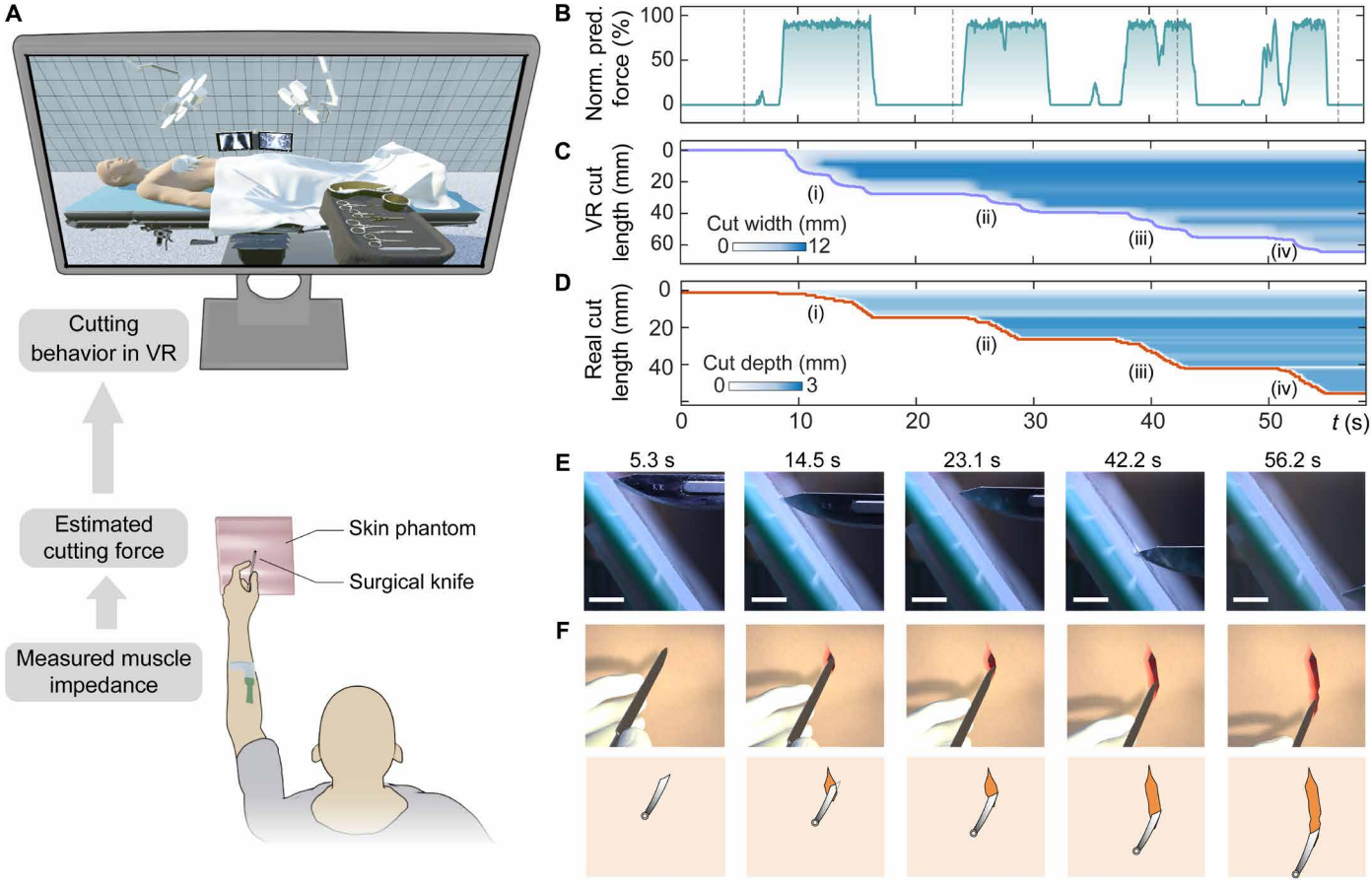


Fig. 6. VR surgery control based on muscle impedance patterns measured by FMEIS. (**A**) Experimental setup illustrating the transmission of muscle force from the human hand cutting a skin phantom to a virtual hand in VR surgery. (**B**) Cutting forces predicted by FMEIS (normalized to a maximal cutting force of 14.3 N, as measured by a force sensor). Norm., normalized; Pred., predicted. (**C**) Cut length and width calculated on the basis of the predicted muscle force, which are used to control the virtual cutting process in VR surgery. (**D**) Real-world cut length and depth captured by a camera. (**E**) Real-world cutting scenes at five time stamps corresponding to the gray dashed lines in (B) showing the knife's position and cutting depth. Scale bars, 1 cm. (**F**) Virtual cutting scenes displaying the position of the virtual surgical knife and the incision progress.

richer muscle state information compared to conventional electrophysiological methods such as EMG. This extended sensing capability is particularly useful for HMI, where subtle changes in muscle state, including passive elongation, can contribute to system control. To ensure high-fidelity signal acquisition with minimal motion artifacts, the FMEIS is engineered with an ultrathin architecture, low elastic modulus, and durable skin adhesion. These features enable consistent and stable impedance measurements during dynamic movements and prolonged use, supporting reliable integration into real-world HMI systems.

We demonstrated the versatility of the FMEIS in three representative scenarios: human-robot collaboration, exoskeleton control, and virtual surgery. In these applications, the ability to detect nuanced muscle activity is particularly valuable for tasks driven by fine interaction forces rather than large-scale joint motion (*43*). As demonstrated in Fig. 5Ci, EMG measurements can be conducted alongside electrical impedance sensing with negligible interference, as the sampling frequency of the former is typically below 2 kHz, while the latter operates at 50 kHz. According to Hill's muscle model (*7*), muscle force is influenced by both muscle activation level and contraction state (muscle length and contraction speed). Therefore, the proposed FMEIS could potentially be integrated with EMG sensors to provide comprehensive muscle force detection in future research.

On the basis of our experimental results, EIMs did not produce any adverse effects on the skin of human participants, even after dozens of tests, each lasting 1 to 2 hours. No participants reported skin irritation or allergic reactions. As noted in several studies (*44*, *45*), bidirectional currents have negligible effects on skin tissue because electrons injected during the negative phases are immediately neutralized by the following positive phases. Furthermore, small-amplitude, high-frequency currents are unlikely to trigger neural activity, as demonstrated both numerically and experimentally in several studies (*46*, *47*). Therefore, the sinusoidal currents used during impedance measurements did not induce muscle contractions or sensory responses. These results suggest that FMEIS can offer safe and noninvasive long-term monitoring for applications in daily life or medical fields.

Although the effectiveness of the FMEIS has been demonstrated across three HMI applications, several challenges remain. One limitation of the current design is the need to retrain the gesture classification

and force regression models each time a new electrode pad is applied to the skin. This is primarily due to the difficulty in positioning the electrode pad in exactly the same location, even with positioning aids. However, transfer learning techniques (*48*, *49*) could potentially reduce the training time when pad placement variations are minor and spatial features remain largely unchanged. Another challenge lies in the difficulty of reconstructing an accurate conductivity image of the participant's forearm for more advanced medical applications. This is due to complex boundary deformations and the limited number of electrodes available (*50*, *51*). In the future, we aim to develop a flexible sensor system that integrates muscle impedance measurement with skin shape sensing to overcome these obstacles in conductivity image reconstruction.

MATERIALS AND METHODS

Flexible sensor pad fabrication

The conductive trace layer was dispense-printed (Hyrel Engine SR, USA) using silver paste S743 (Asahi Solder Pte. Ltd., Singapore) onto a glass substrate covered with Teflon film. The traces were cured in an oven at 110°C for 40 min. To make the encapsulation layers adhesive enough to bond both the conductive traces and human skin, 80% PEIE (Sigma-Aldrich, USA) was used to modify PDMS (SYLGARD 184, Dow Corning, USA) in a ratio of 30 μl of PEIE to 10 g of PDMS. The modified PDMS solution was manually stirred for 3 min and then placed in a vacuum chamber to remove bubbles. It was subsequently spin coated onto the cured conductive traces to form an encapsulation layer ~100 μm thick. The PDMS layer was cured in an oven at 90°C for 1 hour. Once cured, the modified PDMS layer bonded with the conductive traces could be easily peeled off from the Teflon surface, effectively transferring the conductive trace layer to the PDMS. A flexible printed cable was then connected to the conductive traces using the same silver paste, serving as an interface with the driving/sampling PCB. The connection area was sealed with silicone rubber adhesive (K-705, Kafuter, China). A thin PDMS encapsulation layer was manually brushed over the conductive traces, leaving the electrode regions exposed. The hydrogel electrodes were fabricated using a UV-curable double-network hydrogel (*30*). The hydrogel was formulated with AAm, AAc, poly(ethylene glycol) diacrylate (PEGDA), diphenyl (2,4,6-trimethylbenzoyl) phosphine oxide (TPO), and NaCl, all purchased from Sigma-Aldrich. For the hydrogel precursor, AAc (15 wt % of AAm), PEGDA (1 wt % of AAm), and NaCl (5 wt % of AAm) were added to deionized water at an AAm-to-water ratio of 0.35:0.65 and stirred to achieve a homogeneous and transparent solution. TPO (0.5 wt % of AAm) was then added to the solution and stirred for 8 hours until a uniform precursor was obtained.

EIM hardware

We developed both wired and wireless versions of the driving/sampling hardware for muscle impedance measurement. The wired version offers a higher impedance-pattern update rate, while the wireless version is designed for wearable applications. In the wired setup, a signal generator (DG4062, Rigol, China) and a voltage-controlled current source (CS580, SRS, USA) were used in tandem to generate an excitation current of 50 kHz with a typical amplitude of 0.4 mA. The WF3132 multiplexer (WireFlow, Sweden) switched the excitation and measurement channels, while the NI-9223 module (National Instruments, USA) sampled the voltage signals between the electrodes at a frequency of 800 kHz. The timing of the WF3132 and NI-9223 was managed by a real-time controller (cRIO-9053, National Instruments, USA). Details of the design schematics used for sampling the impedance pattern are provided in note S9. The overall update rate of the impedance pattern in the wired version was 112 ms (equivalent to an update frequency of 8.9 Hz).

The wireless PCB version used in this study was based on the circuit schematic from (*26*, *52*, *53*) and the measurement configurations in (*54*). The voltage-controlled current source, composed of a signal generator (AD5930) and two symmetric operational amplifiers (ADA4841), generated an excitation current with the same frequency and amplitude as that of the wired-version hardware. The excitation and measurement channels were switched by four ADG731 multiplexers. Each pair of measuring electrodes was connected to an amplifier chip (AD8220) before being sampled by an analog-to-digital converter (ADS901E). A microcontroller (DEV-15583) configured the components and transmitted the processed impedance pattern to a remote computer via a Bluetooth module (HM-18). Low-dropout voltage regulators were used to supply power to the chips on the PCB, and decoupling capacitors were placed near each chip's power input to ensure voltage stability (fig. S11). In addition, the high operating frequency of the microcontroller (600 MHz) enables stable signal processing and impedance data acquisition over extended periods. As a result, the wireless system maintains signal accuracy and a signal-to-noise ratio comparable to those of the wired system, even after prolonged operation. The entire PCB, powered by a rechargeable 5-V, 1500-mAh battery, weighed 53 g, including the battery. The PCB can operate continuously for ~7 hours when the microcontroller runs at 600 MHz. Details of the design schematics used for sampling the impedance pattern are provided in note S9. For the wireless version, the impedance pattern update rate was 127 ms (equivalent to an update frequency of 7.9 Hz). The update rate is comparable to that of state-of-the-art surgical robot systems (*55*).

The impedance measurement hardware transmitted the impedance patterns to a host computer, where a machine learning algorithm (coded in MATLAB) predicted human gestures and muscle force from the impedance patterns. On the basis of this predicted human information, the host computer sent control signals to the target machine (robot, exoskeleton, or virtual environment).

Grasp force and EMG measurement

Two force sensors were used to measure the grasp force of the human hand, the drilling force of the robotic hand, and the grasp force of the hand exoskeleton: the SBT674 (20 kg; SIMBATOUCH, China) and the DYLY-103 (10 kg; CALT Sensor, China). Forearm muscle EMG signals were recorded using the wireless Trigno Avanti EMG sensor (Delsys, USA). With an operating frequency of 1.926 kHz, the EMG sensor operates well below the FMEIS frequency (50 kHz), ensuring no interference between the two systems.

Setups for robot, exoskeleton, and virtual surgery

For the human-robot collaboration, the robotic hand (Ti5 robot, China) had six df, including the flexion and extension of five fingers, as well as the adduction and abduction of the thumb. The robotic hand was mounted on a six-df robotic arm (CR3, Dobot, China). The robotic hand-arm system was controlled by the host computer via Transmission Control Protocol/Internet Protocol (TCP/IP) and RS485 protocols. In the exoskeleton application, digital control commands were converted to analog air pressures using a functional voltage generator

(DG4062, Rigol, China) and a pressure-regulating valve (ITV2050-312L, SMC Pneumatics, USA). Specifically, the voltage generator translated the digital commands from the host computer into analog voltage signals, which were used to regulate the valve pressure. For the virtual surgery application, the virtual environment was developed using Unity software installed on the host computer. The motions of the virtual knife, hand, and patient skin were updated in real time based on the predicted human motions using a machine learning algorithm implemented in MATLAB.

Human research participants and ethics

The three recruited human participants (average age: 27.6 years) provided informed consent for all experiments and the use of identifiable images in this work. EIMs and human-machine collaboration experiments involving the participants were conducted in accordance with protocols approved by the Ethical Committee of Nanyang Technological University (approval number: IRB-2022-052). All experimental procedures adhered to the principles outlined in the Declaration of Helsinki.

Statistical analysis

The ANOVA and *F* test in Fig. 3 and fig. S10 were conducted with MATLAB. Before the tests, the normality of impedance data distributions was verified with a Kolmogorov-Smirnov normality test.

Supplementary Materials

The PDF file includes:
Supplementary Text
Notes S1 to S9
Tables S1 and S2
Figs. S1 to S12
Legends for movies S1 to S4

Other Supplementary Material for this manuscript includes the following:
Movies S1 to S4

REFERENCES AND NOTES

1. G. Gu, N. Zhang, H. Xu, S. Lin, Y. Yu, G. Chai, L. Ge, H. Yang, Q. Shao, X. Sheng, X. Zhu, X. Zhao, A soft neuroprosthetic hand providing simultaneous myoelectric control and tactile feedback. *Nat. Biomed. Eng.* **7**, 589–598 (2023).
2. T. Chen, X. Yang, B. Zhang, J. Li, J. Pan, Y. Wang, Scale-inspired programmable robotic structures with concurrent shape morphing and stiffness variation. *Sci. Robot.* **9**, eadl0307 (2024).
3. X. Yang, Y. Chen, T. Chen, J. Li, Y. Wang, Active fabrics with controllable stiffness for robotic assistive interfaces. *Adv. Mater.* **36**, 2404502 (2024).
4. S. Luo, M. Jiang, S. Zhang, J. Zhu, S. Yu, I. Dominguez Silva, T. Wang, E. Rouse, B. Zhou, H. Yuk, X. Zhou, H. Su, Experiment-free exoskeleton assistance via learning in simulation. *Nature* **630**, 353–359 (2024).
5. D. Aldarondo, J. Merel, J. D. Marshall, L. Hasenclever, U. Klibaite, A. Gellis, Y. Tassa, G. Wayne, M. Botvinick, B. P. Ölveczky, A virtual rodent predicts the structure of neural activity across behaviors. *Nature* **632**, 594–602 (2024).
6. M. Alaker, G. R. Wynn, T. Arulampalam, Virtual reality training in laparoscopic surgery: A systematic review & meta-analysis. *Int. J. Surg.* **29**, 85–94 (2016).
7. D. Haeufle, M. Günther, A. Bayer, S. Schmitt, Hill-type muscle model with serial damping and eccentric force–velocity relation. *J. Biomech.* **47**, 1531–1536 (2014).
8. L. Tian, B. Zimmerman, A. Akhtar, K. J. Yu, M. Moore, J. Wu, R. J. Larsen, J. W. Lee, J. Li, Y. Liu, B. Metzger, S. Qu, X. Guo, K. E. Mathewson, J. A. Fan, J. Cornman, M. Fatina, Z. Xie, Y. Ma, J. Zhang, Y. Zhang, F. Dolcos, M. Fabiani, G. Gratton, T. Bretl, L. J. Hargrove, P. V. Braun, Y. Huang, J. A. Rogers, Large-area MRI-compatible epidermal electronic interfaces for prosthetic control and cognitive monitoring. *Nat. Biomed. Eng.* **3**, 194–205 (2019).
9. S. Yang, J. Cheng, J. Shang, C. Hang, J. Qi, L. Zhong, Q. Rao, L. He, C. Liu, L. Ding, M. Zhang, S. Chakrabarty, X. Jiang, Stretchable surface electromyography electrode array patch for tendon location and muscle injury prevention. *Nat. Commun.* **14**, 6494 (2023).
10. J. Yin, S. Wang, T. Tat, J. Chen, Motion artefact management for soft bioelectronics. *Nat. Rev. Bioeng.* **2**, 541–558 (2024).
11. A. Moin, A. Zhou, A. Rahimi, A. Menon, S. Benatti, G. Alexandrov, S. Tamakloe, J. Ting, N. Yamamoto, Y. Khan, F. Burghardt, L. Benini, A. C. Arias, J. M. Rabaey, A wearable biosensing system with in-sensor adaptive machine learning for hand gesture recognition. *Nat. Electron.* **4**, 54–63 (2021).
12. D. Pereira Botelho, K. Curran, M. M. Lowery, Anatomically accurate model of EMG during index finger flexion and abduction derived from diffusion tensor imaging. *PLOS Comput. Biol.* **15**, e1007267 (2019).
13. M. L. Latash, *Fundamentals of Motor Control* (Academic Press, 2012).
14. M. Gherardini, V. Ianniciello, F. Masiero, F. Paggetti, D. D'Accolti, E. La Frazia, O. Mani, S. Dalise, K. Dejanovic, N. Fragapane, L. Maggiani, E. Ipponi, M. Controzzi, M. Nicastro, C. Chisari, L. Andreani, C. Cipriani, Restoration of grasping in an upper limb amputee using the myokinetic prosthesis with implanted magnets. *Sci. Robot.* **9**, eadp3260 (2024).
15. M. Shahmohammadi, B. Guan, R. V. Godoy, A. Dwivedi, P. Nielsen, M. Liarokapis, On lightmyography based muscle-machine interfaces for the efficient decoding of human gestures and forces. *Sci. Rep.* **13**, 327 (2023).
16. Y. Ling, X. Chen, Y. Ruan, X. Zhang, X. Chen, Comparative study of gesture recognition based on accelerometer and photoplethysmography sensor for gesture interactions in wearable devices. *IEEE Sens. J.* **21**, 17107–17117 (2021).
17. R. Tchantchane, H. Zhou, S. Zhang, G. Alici, A review of hand gesture recognition systems based on noninvasive wearable sensors. *Adv. Intell. Syst.* **5**, 2300207 (2023).
18. C. Wang, X. Chen, L. Wang, M. Makihata, H.-C. Liu, T. Zhou, X. Zhao, Bioadhesive ultrasound for long-term continuous imaging of diverse organs. *Science* **377**, 517–523 (2022).
19. H. Hu, H. Huang, M. Li, X. Gao, L. Yin, R. Qi, R. S. Wu, X. Chen, Y. Ma, K. Shi, C. Li, T. M. Maus, B. Huang, C. Lu, M. Lin, S. Zhou, Z. Lou, Y. Gu, Y. Chen, Y. Lei, X. Wang, R. Wang, W. Yue, X. Yang, Y. Bian, J. Mu, G. Park, S. Xiang, S. Cai, P. W. Corey, J. Wang, S. Xu, A wearable cardiac ultrasound imager. *Nature* **613**, 667–675 (2023).
20. M. Lin, Z. Zhang, X. Gao, Y. Bian, R. S. Wu, G. Park, Z. Lou, Z. Zhang, X. Xu, X. Chen, A. Kang, X. Yang, W. Yue, L. Yin, C. Wang, B. Qi, S. Zhou, H. Hu, H. Huang, M. Li, Y. Gu, J. Mu, A. Yang, A. Yaghi, Y. Chen, Y. Lei, C. Lu, R. Wang, J. Wang, S. Xiang, E. B. Kistler, N. Vasconcelos, S. Xu, A fully integrated wearable ultrasound system to monitor deep tissues in moving subjects. *Nat. Biotechnol.* **42**, 448–457 (2024).
21. X. Gao, X. Chen, M. Lin, W. Yue, H. Hu, S. Qin, F. Zhang, Z. Lou, L. Yin, H. Huang, S. Zhou, Y. Bian, X. Yang, Y. Zhu, J. Mu, X. Wang, G. Park, C. Lu, R. Wang, R. S. Wu, J. Wang, J. Li, S. Xu, A wearable echomyography system based on a single transducer. *Nat. Electron.* **7**, 1035–1046 (2024).
22. H. Hu, Y. Ma, X. Gao, D. Song, M. Li, H. Huang, X. Qian, R. Wu, K. Shi, H. Ding, M. Lin, X. Chen, W. Zhao, B. Qi, S. Zhou, R. Chen, Y. Gu, Y. Chen, Y. Lei, C. Wang, C. Wang, Y. Tong, H. Cui, A. Abdal, Y. Zhu, X. Tian, Z. Chen, C. Lu, X. Yang, J. Mu, Z. Lou, M. Eghtedari, Q. Zhou, A. Oberai, S. Xu, Stretchable ultrasonic arrays for the three-dimensional mapping of the modulus of deep tissue. *Nat. Biomed. Eng.* **7**, 1321–1334 (2023).
23. C. A. Shiffman, Pre-contraction dynamic electrical impedance myography of the forearm finger flexors. *Physiol. Meas.* **37**, 291–313 (2016).
24. B. Sanchez, J. Li, T. Geisbush, R. B. Bardia, S. B. Rutkove, Impedance alterations in healthy and diseased mice during electrically induced muscle contraction. *IEEE Trans. Biomed. Eng.* **63**, 1602–1612 (2016).
25. E. Zheng, Y. Li, Z. Zhao, Q. Wang, H. Qiao, An electrical impedance tomography based interface for human–robot collaboration. *IEEE/ASME Trans. Mechatron.* **26**, 2373–2384 (2021).
26. J. Zhu, Y. Lei, A. Shah, G. Schein, H. Ghaednia, J. Schwab, C. Harteveld, S. Mueller, paper presented at the 35th Annual ACM Symposium on User Interface Software and Technology, Bend, OR, USA, October 29 2022.
27. G. Ma, Z. Hao, X. Wu, X. Wang, An optimal electrical impedance tomography drive pattern for human-computer interaction applications. *IEEE Trans. Biomed. Circuits Syst.* **14**, 402–411 (2020).
28. A. Kalra, A. Lowe, A. M. Al-Jumaily, Mechanical behaviour of skin: A review. *J. Mater. Sci. Eng.* **5**, 1000254 (2016).
29. S. H. Jeong, Z. Shou, K. Hjort, J. Hilborn, Z. Wu, PDMS-based elastomer tuned soft, stretchable, and sticky for epidermal electronics. *Adv. Mater.* **28**, 5830–5836 (2016).
30. K. Wu, J. Li, Y. Li, H. Wang, Y. Zhang, B. Guo, J. Yu, Y. Wang, 3D printed silk fibroin-based hydrogels with tunable adhesion and stretchability for wearable sensing. *Adv. Funct. Mater.* **34**, 2404451 (2024).
31. R. Maiti, L.-C. Gerhardt, Z. S. Lee, R. A. Byers, D. Woods, J. A. Sanz-Herrera, S. E. Franklin, R. Lewis, S. J. Matcher, M. J. Carré, In vivo measurement of skin surface strain and sub-surface layer deformation induced by natural tissue stretching. *J. Mech. Behav. Biomed. Mater.* **62**, 556–569 (2016).
32. A. Karwoski, R. Plaut, Experiments on peeling adhesive tapes from human forearms. *Skin Res. Technol.* **10**, 271–277 (2004).
33. F. H. Netter, *Atlas of Human Anatomy* (Saunders Elsevier, 2014).
34. S. Gabriel, R. W. Lau, C. Gabriel, The dielectric properties of biological tissues: II. Measurements in the frequency range 10 Hz to 20 GHz. *Phys. Med. Biol.* **41**, 2251–2269 (1996).

35. T. K. Bera, J. Nagaraju, Studying the resistivity imaging of chicken tissue phantoms with different current patterns in electrical impedance tomography (EIT). *Measurement* **45**, 663–682 (2012).
36. T. J. Cleophas, A. H. Zwinderman, *Statistics Applied to Clinical Studies* (Springer Science & Business Media, 2012).
37. L. Tang, J. Shang, X. Jiang, Multilayered electronic transfer tattoo that can enable the crease amplification effect. *Sci. Adv.* **7**, eabe3778 (2021).
38. A. Tashakori, Z. Jiang, A. Servati, S. Soltanian, H. Narayana, K. Le, C. Nakayama, C.-l. Yang, Z. J. Wang, J. J. Eng, Capturing complex hand movements and object interactions using machine learning-powered stretchable smart textile gloves. *Nat. Mach. Intell.* **6**, 106–118 (2024).
39. C. Papadimitriou, C. P. Fritzen, P. Kraemer, E. Ntotsios, Fatigue predictions in entire body of metallic structures from a limited number of vibration sensors using Kalman filtering. *Struct. Control Health Monit.* **18**, 554–573 (2011).
40. M. Cifrek, V. Medved, S. Tonković, S. Ostojić, Surface EMG based muscle fatigue evaluation in biomechanics. *Clin. Biomech.* **24**, 327–340 (2009).
41. J. Troccaz, G. Dagnino, G.-Z. Yang, Frontiers of medical robotics: From concept to systems to clinical translation. *Annu. Rev. Biomed. Eng.* **21**, 193–218 (2019).
42. S. Jadhav, M. R. A. Majit, B. Shih, J. P. Schulze, M. T. Tolley, Variable stiffness devices using fiber jamming for application in soft robotics and wearable haptics. *Soft Robot.* **9**, 173–186 (2022).
43. R. Miyazaki, K. Hirose, Y. Ishikawa, T. Kanno, K. Kawashima, A master–slave integrated surgical robot with active motion transformation using wrist axis. *IEEE/ASME Trans. Mechatron.* **23**, 1215–1225 (2018).
44. J. Malmivuo, R. Plonsey, *Bioelectromagnetism - Principles and Applications of Bioelectric and Biomagnetic Fields* (Oxford Univ. Press, 1995).
45. H. A. Abu-Khaber, A. M. Z. Abouelela, E. M. Abdelkarim, Effect of electrical muscle stimulation on prevention of ICU acquired muscle weakness and facilitating weaning from mechanical ventilation. *Alex. J. Med.* **49**, 309–315 (2013).
46. J. Li, K.-M. Lee, K. Bai, Analytical and experimental investigation of temporal interference for selective neuromuscular activation. *IEEE Trans. Neural Syst. Rehabil. Eng.* **28**, 3100–3112 (2020).
47. D. Serrano-Muñoz, J. Avendaño-Coy, C. Simón-Martínez, J. Taylor, J. Gómez-Soriano, Effect of high-frequency alternating current transcutaneous stimulation over muscle strength: A controlled pilot study. *J. Neuroeng. Rehabil.* **15**, 1–4 (2018).
48. J. Li, K.-M. Lee, Muscle-driven joint-torque estimation based on voltage-torque mapping of electrical impedance sensing. *IEEE Sens. J.* **23**, 13966–13977 (2023).
49. D. Yang, H. Liu, An EMG-based deep learning approach for multi-DoF wrist movement decoding. *IEEE Trans Ind Electron* **69**, 7099–7108 (2022).
50. P. A. Sejati, B. Sun, P. N. Darma, T. Shirai, K. Narita, M. Takei, Multi-node electrical impedance tomography (*mn*EIT) throughout whole-body electrical muscle stimulation (*wb*EMS). *IEEE Trans. Instrum. Meas.* **72**, 1–14 (2023).
51. Y. Wu, D. Jiang, X. Liu, R. Bayford, A. Demosthenous, A human–machine interface using electrical impedance tomography for hand prosthesis control. *IEEE Trans. Biomed. Circuits Syst.* **12**, 1322–1333 (2018).
52. A. S. Tucker, R. M. Fox, R. J. Sadleir, Biocompatible, high precision, wideband, improved howland current source with lead-lag compensation. *IEEE Trans. Biomed. Circuits Syst.* **7**, 63–70 (2013).
53. A. Adler, D. Holder, *Electrical Impedance Tomography: Methods, History and Applications* (CRC Press, 2021).
54. J. Li, K.-M. Lee, A novel method for soft contact sensing based on electrical impedance sensitivity images. *IEEE Sens. J.* **22**, 9296–9305 (2022).
55. M. Kibsgaard, M. Kraus, paper presented at the International Conference on Computer Graphics Theory and Applications, Porto, Portugal, February 27 2017.

Acknowledgments: We express our appreciation to Y. Liu, Y. Yang, Y. He, J. Su, and C. Linghu for the support in experiments. We also thank our laboratory colleagues B. Zhang, W. Mao, and Z. Meng for the advice during the experiments. **Funding:** We acknowledge the support by the A*STAR Singapore through RIE2025 MTC IRG Award M21K2c0118. Y.W. acknowledges the NAP award (020482) from Nanyang Technological University, Singapore. **Author contributions:** Conceptualization: J.L. and Y.W. Methodology: J.L., K.W., J.X., and Y.W. Software: J.L. Validation: J.L., K.W., and Y.W. Formal analysis: J.L. and K.W. Investigation: J.L., K.W., J.X., T.C., X.Y., J.P., and Y.C. Resources: J.L. and Y.W. Data curation: J.L. Visualization: J.L. and K.W. Supervision: Y.W. Writing—original draft: J.L., K.W., and Y.W. Writing—review and editing: J.L., K.W., and Y.W. Project administration: J.L. and Y.W. Funding acquisition: Y.W. **Competing interests:** The authors declare that they have no competing interests. **Data and materials availability:** All data needed to evaluate the conclusions in the paper are present in the paper and/or the Supplementary Materials.

Submitted 16 December 2024
Accepted 21 May 2025
Published 27 June 2025
10.1126/sciadv.adv3359

ScienceAdvances

Flexible multichannel muscle impedance sensors for collaborative human-machine interfaces

Junwei Li, Kunlin Wu, Jingcheng Xiao, Tianyu Chen, Xudong Yang, Jie Pan, Yu Chen, and Yifan Wang

Sci. Adv. **11** (26), eadv3359. DOI: 10.1126/sciadv.adv3359

View the article online
https://www.science.org/doi/10.1126/sciadv.adv3359
Permissions
https://www.science.org/help/reprints-and-permissions

Use of this article is subject to the Terms of service

Science Advances (ISSN 2375-2548) is published by the American Association for the Advancement of Science. 1200 New York Avenue NW, Washington, DC 20005. The title *Science Advances* is a registered trademark of AAAS.

Copyright © 2025 The Authors, some rights reserved; exclusive licensee American Association for the Advancement of Science. No claim to original U.S. Government Works. Distributed under a Creative Commons Attribution NonCommercial License 4.0 (CC BY-NC).